ACS OMEGA

Open Access

http://pubs.acs.org/journal/acsodf

Article

Study on the Influence Mechanism of Hot Flue Gas Injection Pressure on the Wettability of Anthracite Coal: From the Perspective of Molecular Dynamics

Shunqing Ma, Baiquan Lin,* Xiangliang Zhang,* Qian Liu, and Wei Zha

Cite This: *ACS Omega* 2024, 9, 44577−44587

Read Online

ACCESS | Metrics & More | Article Recommendations

ABSTRACT: A multicomponent wetting model of coal−water−methane−hot flue gas was hereby constructed to investigate the influence of complex components of hot flue gas on coal wettability. Besides, whether it is feasible to use the NIST method to capture the system pressure was verified from a microscopic perspective. Moreover, how the interaction energy and hydrogen bonds between water and coal, the spreading length of water nanodroplets in the *X*-direction, and the three-phase contact angle vary with the hot flue gas injection pressure were discussed. Here are the findings: (1) The absolute value of interaction energy between water and coal is negatively correlated with the pressure. In addition, the gradient of decrease shrinks continuously when the pressure rises. (2) As the pressure rises, a decline is monitored in both the number of hydrogen bonds and the spreading length of water nanodroplets in the *X*-direction, and a critical pressure value exists around 32.64 MPa, which divides the variation into two stages, i.e., rapid decrease and slow decrease. (3) The three-phase contact angle grows with the rise of pressure, and its critical pressure value is similar to that of number of hydrogen bonds and spreading length. In addition, it is found that the density of the gas adsorption layer augments as the pressure rises, which can be seen that a higher injection pressure is favorable for gas wetting. These research observations brought to light that appropriately raising the hot flue gas injection pressure can promote the transition of wetting mode from water wetting to gas wetting, which is of great benefit for relieving the water lock effect and effectively improving the transportation environment of gas.

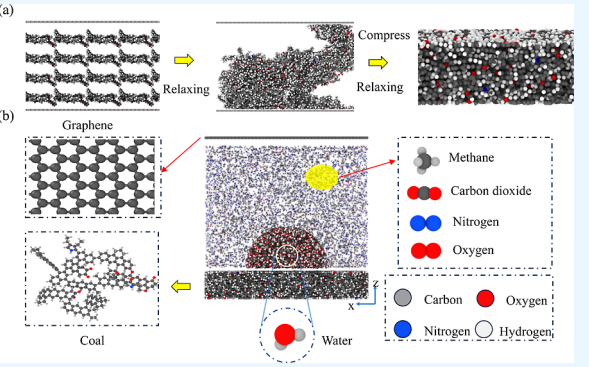

1. INTRODUCTION

China boasts an abundant reserve of deep coalbed methane (CBM), yet most of its coal reservoirs are faced with such problems as high stress, low permeability, and strong adsorption, which poses a serious threat to the efficient extraction of CBM.[1,2] In recent years, the use of hot flue gas generated by gas thermal power plants to enhance CBM extraction in low-permeability and high-adsorption coal seams has attracted considerable attention. Hot flue gas is mainly composed of N_2, CO_2, H_2O, and a small amount of O_2. If emitted in large amounts, it would exacerbate the greenhouse effect and bring about resource waste. However, the good thing is that if it is injected into coal reservoirs after being captured, the desorbed gas flow can be well boosted, thus increasing CBM production, achieving CO_2 geological storage, and alleviating the greenhouse effect.

Methods of permeability enhancement such as hydraulic fracturing, hydraulic cutting, and hydraulic punching have seen extensive application and made encouraging achievements in coal production. Given this, they are acknowledged as important coal reservoir modification technologies.[3,4] A case in point is the attempt made by Li et al. and Zhou et al. They combined hydraulic fracturing with hydraulic cutting to obtain more uniform fracture distribution networks.[5] Additionally, coal reservoirs are considered ideal sites for carbon sequestration. For example, in the San Juan Basin, nearly 6.4 billion cubic feet of CO_2 was injected into the reservoir through the Allison device, inducing an approximately 18% increase in CBM production. Zhang et al.[6] conducted CO_2-enhanced CBM recovery (CO_2-ECBM) experiments on bituminous coal under an injection pressure of 6−10 MPa, in which the CO_2 injection rate, the CH_4 displacement rate, and the coal volumetric strain rate were taken into account. They reported that a high CO_2 injection pressure would give rise to coal swelling and deformation, thus lowering permeability and CH_4 production.

Received: July 30, 2024
Revised: September 29, 2024
Accepted: October 16, 2024
Published: October 23, 2024

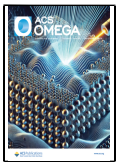

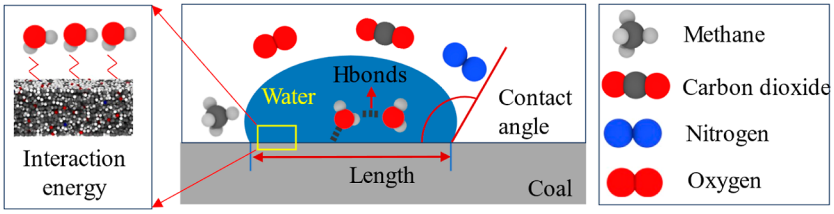

Figure 1. Key parameters for characterizing the wettability of coal.

Compared with the above methods, the injection of hot flue gas, which features the coupling of the thermal effect, the dissolution effect, and the displacement effect, is capable of addressing the problems of high adsorption and low permeability, hence significantly enhancing the performance of CBM extraction.

With a view to further elucidating the mechanism of enhancing permeability and displacing low-permeability and high-adsorption coal reservoirs with hot flue gas, many studies have been carried out at home and abroad. At the same temperature, the adsorption affinity of the coal matrix for fluids falls on the following order: CO_2 > CH_4 > N_2, and such a difference can be explained from the perspectives of free energy, adsorption potential, adsorption heat, and functional theory.[7−9] Apart from this, a higher stagnation temperature[10] and a higher pore entry rate[11] also endow CO_2 with stronger adsorption capacity in the coal reservoir. Jessen et al.[12] performed displacement experiments on coal by injecting CO_2, N_2, and CO_2/N_2 mixtures with different mass ratios, and the experimental results revealed that the initial CH_4 recovery rate increases as the volume fraction of N_2 expands. Wang et al.[13] launched gas−water two-phase displacement experiments using a self-developed high-temperature triaxial platform, and drew a conclusion that heating the coal reservoir can accelerate water desorption (30−120 °C for surface water of coal particles and 120−180 °C for capillary water), thereby opening up more seepage channels for CBM and increasing gas production. In the process of hot flue gas injection, the expansion deformation of coal mainly includes thermal expansion caused by temperature rise and gas adsorption-induced expansion. Su et al.[14] explored the influence of thermal expansion-induced deformation on coal permeability during the heating process from 30 to 150 °C, and concluded that the thermal expansion-induced deformation of coal becomes less sensitive to temperature with the rise of temperature. Chen et al.[15] found that the interaction between SC−CO_2 and coal leads to a decrease in carbonate minerals, kaolinite, and pyrite, further triggering the opening of closed or semiclosed pores. Kaveh et al.[16] tested the wettability of coal surface in the flue gas system which was composed of bituminous coal (Warndt Luisenthal coal), water, N_2, and CO_2. Their results suggested that the static contact angle grows linearly with the rise of pressure, and the coal surface becomes hydrophobic when the pressure exceeds 8.5 MPa.

Wettability is viewed as a critical factor controlling capillary force, CO_2 adsorption, and methane transportation, which directly impacts the effectiveness of hot flue gas displacement for CBM and the capacity of CO_2 geological storage. Since pressure plays a decisive role in changing the wettability, there is an urgent need to figure out how hot flue gas injection pressure influences the wettability of coal. Compared with low-rank coal, high-rank coal, especially high-rank anthracite, possesses a more complex pore structure and a higher gas content. Moreover, it is considered to boast a more suitable engineering background in the application of hot flue gas. However, existing research has mostly focused on the wettability of coal−water−CO_2 systems or SiO_2[17,18] and kerogen molecules, while scarce attention is paid to this regard. To address this problem, the molecular dynamics (MD) simulation method is adopted in this study to construct a multicomponent wetting model of coal−water−methane-hot flue gas. As shown in Figure 1, key parameters for characterizing the wettability of coal, including interaction energy between coal and water, number of hydrogen bonds between coal and water, spreading length of water droplets in the *X*-direction, and three-phase contact angle, are researched in an effort to reveal the influence mechanism of hot flue gas injection pressure on the wettability of coal. In addition, whether it is feasible to adopt the NIST method to obtain the system pressure is also verified from a microscopic perspective.

2. METHODS

2.1. Force Field Theory. In this study, the DREDING force field,[19,20] as a commonly used universal force field, can accurately describe properties such as intermolecular interactions and thermodynamic properties,[21,22] is adopted to describe the coal macromolecular model. It is developed based on quantum mechanics theory and experimental data, and is often used to describe the interactions between different molecules by describing the energy and force of nonbonds, bonds, angles, and dihedral angles between atoms using a set of parameters. Besides, the structure and composition of coal macromolecules is verified by elemental analysis, Fourier transform infrared spectroscopy, and ^{13}C solid nuclear magnetic resonance (^{13}C NMR) on actual coal samples, and the molecular formula of coal macromolecules is determined as $C_{199}H_{146}N_2O_9$. Furthermore, the density at the most stable configuration is tracked through annealing and geometric optimization.[23] The SPC/E model,[24] which demonstrates excellent performance in characterizing water's structure, interfacial tension,[25,26] dynamic characteristics, and interaction with other molecules over a wide range of pressure, is employed here for simulating the movement of water molecules. In United-atom force field, the relative atomic mass of hydrogen atoms directly bonded to carbon atoms is overlapped on the carbon atom, forming a united atom as a whole. At the same time, the interactions between other atoms and hydrogen atoms are also superimposed on the united atom. Although it can simplify the calculation process and reduce potential parameters, the number of force points is less than the number of atoms, which is an incomplete representation of the molecule and performs poorly in the calculation accuracy of multicomponent complex interactions. Different from existing studies, this study adopts the OPLS-AA[27] force field to describe the motion of methane molecules. The EPM2[28] force field that considers the influence brought by the polarization effect is used here to describe carbon dioxide molecules in the hope of more accurately characterizing the intermolecular interaction. Some scholars believe that in the supercritical state, this model has higher applicability and accuracy compared to other models.[29,30]

https://doi.org/10.1021/acsomega.4c06994
ACS Omega 2024, 9, 44577−44587

On the premise of guaranteeing computational accuracy, nitrogen and oxygen molecules also rely on the DREDING force field, so as to save computational resources. The force field parameters of components in the simulation system are listed in Table 1.

Table 1. Force Field Parameters of Components in the Simulation System

force or charge site	σ (Å)	ε (kcal/mol)	q (e)
water (SPE/C model)			
O	3.165570	0.155400	−0.847600
H	0.000000	0.000000	0.423800
methane (OPLS-AA model)			
C	3.500000	0.066000	−0.541300
H	2.500000	0.030000	0.135300
carbon dioxide (EPM_2 model)			
C	2.757000	0.055899	0.471200
O	3.033000	0.159983	−0.235600
nitrogen (DREDING)			
N	3.260689	0.069000	0.000000
oxygen (DREDING)			
O	3.118146	0.060000	0.000000

2.2. Model Construction. The multicomponent wetting model constructed in this study is composed of coal substrate, water nanodroplets, and hot flue gas (Figure 2). The specific construction process is described as follows.

(1) Coal substrate: First, 96 coal macromolecules are arrayed in a 20 × 5 × 10 nm^3 simulation box using Moltemplate, and a graphene plate is inserted and fixed at both ends of the *Z*-axis. Then, these coal macromolecules are relaxed at 300 K for 200 ps in the *NVT* ensemble controlled by a Nos'e Hoover thermostat,[31] which allows them to stretch between the two graphene plates. Subsequently, the upper graphene plate is unfixed and a downward external force *F* is applied onto it, while the lower graphene plate remains fixed. In this case, the position change of the centroid COM of the upper graphene plate is observed. When the centroid position coordinates becomes basically constant, the relaxation continues for 200 ps, after which the graphene plates are removed. The completed coal substrate is 20 × 5 × 4 nm^3 in size, and its *Z*-direction density distribution is exhibited in Figure 3. As can be seen from Figure 3, the density of the coal substrate fluctuates slightly around 1.47 g/cm^3, the variance being 3.93 × 10^{-3}, which falls within the range of true anthracite density and is consistent with the density at the most stable configuration.

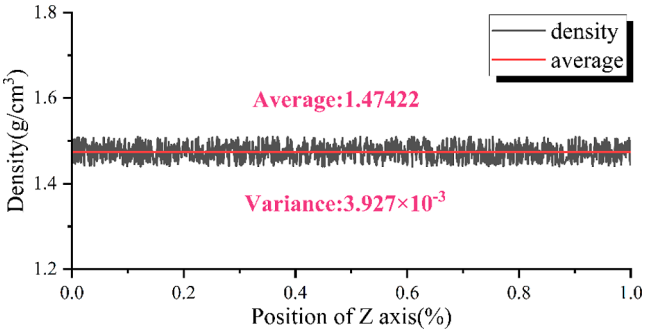

Figure 3. Density distribution of coal.

(2) Water nanodroplets and hot flue gas: It has been found that the interruption of linear tension during the initial movement of water droplets can be effectively minimized if semicylindrical water nanodroplets are used as the initial configuration.[32] The semicylindrical water nanodroplet used in our system comprises 3,500 water molecules with a radius of 5 nm. Similarly, the centerline length is also 5 nm, extending from Point A (10, 0, 0) to Point B (0, 5, 0). In this study, hot flue gas consists of N_2, O_2, and CO_2 whose proportions are 87%, 2.2%, and 10.8%, respectively. These proportions are determined by the chemical equation of methane combustion. The molar ratio between the components is kept unchanged under different pressures, and only the number of molecules varies.

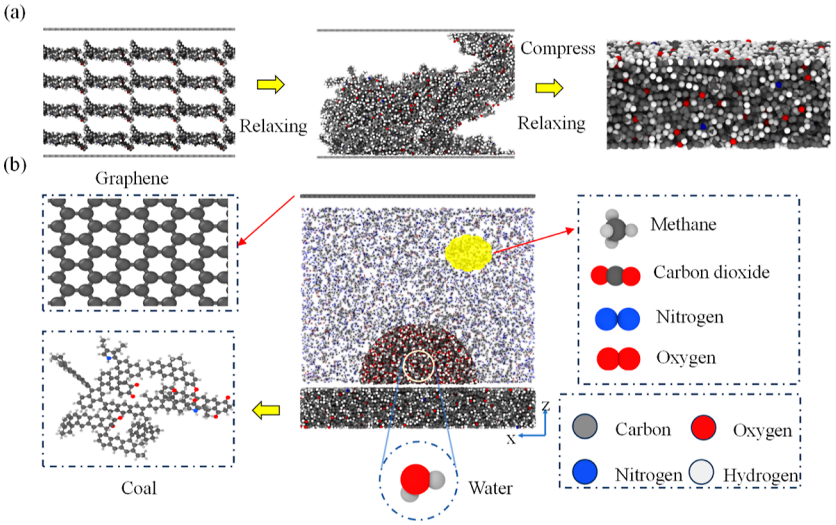

Figure 2. Process for constructing a multicomponent wetting model of coal−water−methane−hot flue gas. (a) The construction process of coal base. (b) Composition of multicomponent wettability model.

https://doi.org/10.1021/acsomega.4c06994
ACS Omega 2024, 9, 44577−44587

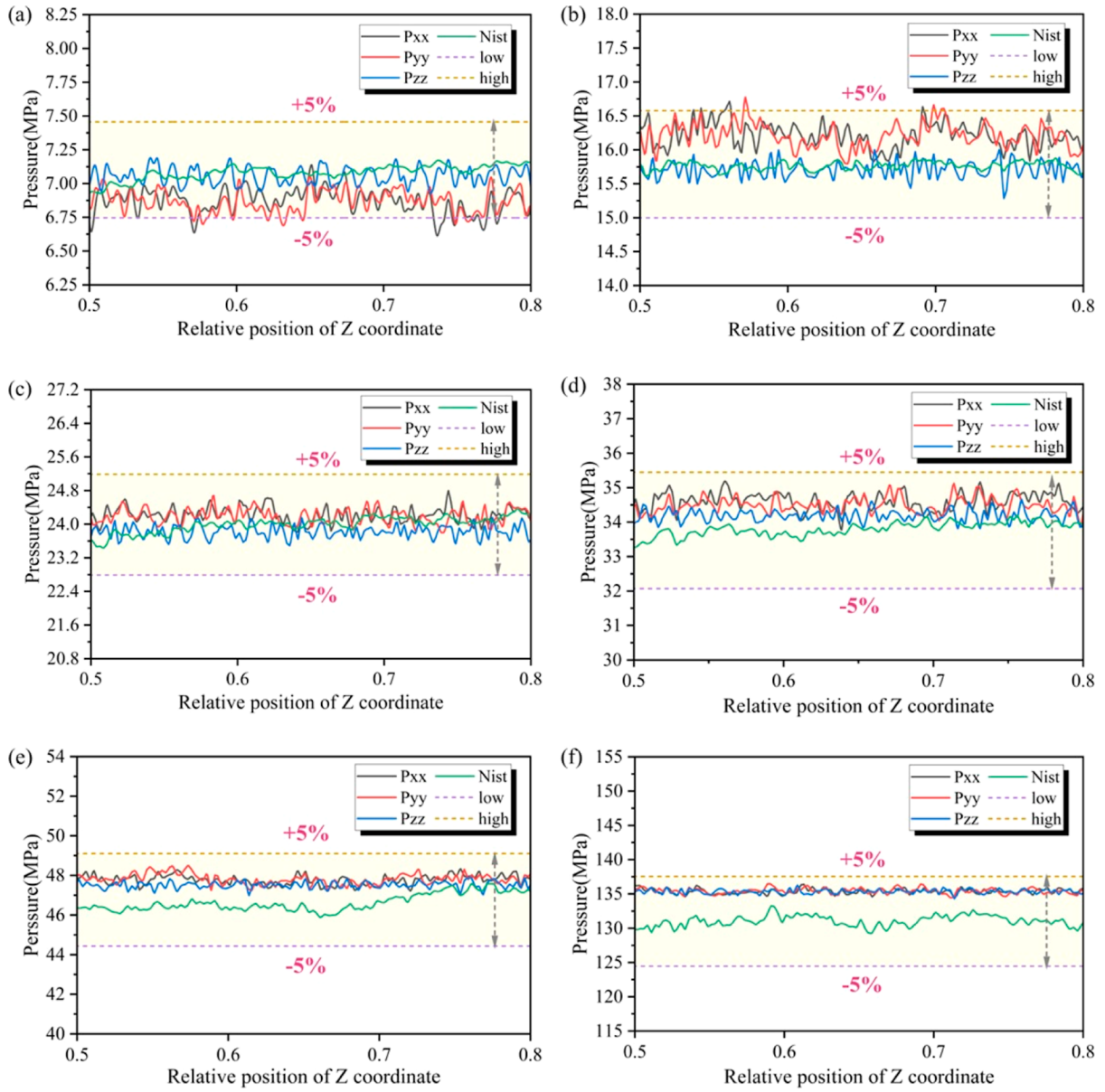

Figure 4. Verification of feasibility of the NIST method. The number of molecules in hot flue gas: (a) 0. (b) 1739. (c) 2475. (d) 5214. (e) 6951. (f) 13900.

(3) Model combination: The water nanodroplets and multicomponent gas are placed on the surface of the coal substrate, and some space is left to prevent excessive interatomic stress in the initial stage of simulation. Next, a rigid graphene plate where gas molecules have nonbonded interactions is inserted onto the top of the *Z*-axis of the model for the purpose of eliminating the disruption of periodic boundary conditions on the density distribution of methane and hot flue gas molecules at the top of the model. The entire model is $20 \times 5 \times 20$ nm^3 in size.

2.3. MD Simulation. The entire simulation is performed using a large-scale atomic/molecular parallel simulator (LAMMPS) package.[33] Water, methane, and hot flue gas are relaxed for 2 ns in the *NVT* ensemble, in which the temperature of water and methane molecules is controlled at 300 K and that of hot flue gas is set to 440 K. After the relaxation comes to an end, the *NVT* ensemble is removed, and the *NVE* ensemble is applied to the entire system for 8 ns, during which the last 2 ns is singled out for subsequent analysis. The time step of the entire simulation is set to 1 fs.

During the simulation, the shake algorithm[34] is exercised to keep water molecules rigid. The nonbonded interactions between atoms are calculated through Leonard Jones (12-6LJ)[35] and short-range Coulomb forces with a cutoff radius of 1.2 nm

$$U(r_{ij}) = 4\varepsilon\left[\left(\frac{\sigma_{ij}}{r_{ij}}\right)^{12} - \left(\frac{\sigma_{ij}}{r_{ij}}\right)^{6}\right] + \frac{q^j q^i}{4\pi\varepsilon_0 r_{ij}} \quad (1)$$

where r_{ij} is the distance between two atoms; ε is the depth of the potential well; and σ_{ij} is the distance between atoms in the case where the LJ potential is 0. The long-range Coulomb force is calculated with the particle-particle-particle-mesh solver, the calculation accuracy being 1×10^{-4}.[36] Meanwhile, the

https://doi.org/10.1021/acsomega.4c06994
ACS Omega 2024, 9, 44577−44587

nonbonded interactions between different kinds of atoms are deduced using the Lorentz−Berthelot mixing rule

$$\sigma_{\alpha\beta} = (\sigma_\alpha + \sigma_\beta)/2 \tag{2}$$

$$\varepsilon_{\alpha\beta} = \sqrt{\varepsilon_\alpha \varepsilon_\beta} \tag{3}$$

where α and β stand for two types of atoms, respectively. The tail correction[37−42] is employed to correct the nonbonded interactions beyond the cutoff radius for pursuit of higher accuracy. A periodic boundary is exerted on the *X*, *Y*, and *Z*-directions of the model, and the coal substrate is set as rigid during the simulation to acquire more precise contact angles.[43]

2.4. Pressure Verification. The reasonable and appropriate setting of pressure, an extremely important variable in molecular simulations, wields a vital role in simulation results. The pressure control method adopted in the *NPT* ensemble is inapplicable to models with a constant volume. Zhou et al.[44] proposed a new method, i.e., filling different numbers of molecules into a fixed volume simulation box to achieve control of the gas phase density, and importing the density into the NIST database to obtain pressure. This method performs well in controlling the pressure in the model without using an *NPT* ensemble. However, whether the nanoscale molecular simulation results are compatible with the experiment-based NIST database remains unclear. As displayed in eq 4, in an isotropic stress state, the diagonal component of stress tensor is consistent with the pressure.

$$\sigma = \begin{pmatrix} -p & 0 & 0 \\ 0 & -p & 0 \\ 0 & 0 & -p \end{pmatrix} \tag{4}$$

where σ is the stress tensor, and $-p$ is the opposite number of pressure. In this study, the macro-micro connections are fully examined by comparing the pressure curve obtained by importing the gas phase density (10−16 nm range on the *Z*-axis) into the NIST database, P_{NIST}, with the three principal stress curves calculated by LAMMPS. The results well demonstrate the feasibility of the above method. It is worth noting that the diagonal components of the three stress tensors calculated by LAMMPS all contain volume terms which should be eliminated before the comparison with P_{NIST}.

The stress is the statistical average of the last 2 ns, whose calculation also relies on molecules in the gas phase. The principal stress curves and P_{NIST} curves under various numbers of gas molecules are depicted in Figure 4. By comparing Figure 4a−d, it is apparent that the principal stress curves intersect with the P_{NIST} curve, both fluctuating consistently within a narrow range. In Figure 4e,f, a slight separation can be observed between the principal stress curves and the P_{NIST} curve. This is because when the bulk molecular density is extremely high, the molecular spacing narrows and the intermolecular repulsion force increases remarkably, which further leads to an overestimation of the principal stress calculated by LAMMPS. In an effort to better illustrate the compatibility between macro and micro results, 105% and 95% of the average value of P_{NIST} are taken as the upper and lower limits of the fluctuation, represented by yellow and purple dashed lines, respectively. In all the simulation results, the principal stress curves fluctuate within the specified upper and lower limits, with a deviation of less than 5% from the average of P_{NIST}. Therefore, it is feasible to regard the pressure values obtained from the NIST database as the system pressure.

According to Dalton's partial pressure method, the hot flue gas injection pressure marks 0, 5.79, 12.88, 21.43, 32.64, and 107.68 MPa when the number of molecules is 0, 1739, 3475, 5214, 6950, and 13,900, respectively (Table 2).

Table 2. Correspondence Between the Number of Different Molecules and the Hot Flue Gas Injection Pressure

P (MPa)	number of H_2O molecules	number of CH_4 molecules	number of CO_2 molecules	number of N_2 molecules	number of O_2 molecules
0	3500	3000	0	0	0
5.79	3500	3000	188	1512	39
12.88	3500	3000	375	2023	77
21.43	3500	3000	563	4535	116
32.64	3500	3000	750	6047	154
107.68	3500	3000	1500	12,094	306

3. RESULTS AND DISCUSSION

3.1. Interaction Energy. The interaction energy between the water droplets and the coal substrate plays an important role in the wetting performance of water droplets. Equation 5 below is employed by many scholars to calculate the interaction energy between two components[45−47]

$$E_{interaction} = E_{AB} - E_A - E_B \tag{5}$$

where E_{AB} is the total energy of the AB system, and E_A and E_B are the energy of substances A and B when either of them exists.

Aiming at acquiring more precise interaction energy between coal and water, a velocity (v) in the negative direction of the *Z*-axis is applied to the coal substrate after the completion of *NVE* ensemble application. However, it should be noted that the velocity (v) applied should not be too large to separate the coal substrate from the water droplets, otherwise gas molecules would fill the gaps and affect the calculation results. On the other hand, the velocity should not be too small, otherwise the energy changes of the system would fail to be accurately captured within a time step. As illustrated in Figure 5b, after the addition of the velocity (v), the water droplets are significantly stretched and move downward with the coal substrate driven by the interaction energy without any detachment. Based on the above analysis, it is concluded that a speed of 1 Å/ps is adequate to meet the simulation requirements. To eliminate the disruption of periodic boundaries, the size of the simulation box is expanded by 150 Å in the positive and negative directions prior to the exertion of the velocity.

The interaction energy curves between coal and water under different hot flue gas pressures are drawn in Figure 5a. These curves demonstrate consistent changes over time under different pressures. Specifically, the interaction energy surges at the moment when the coal substrate starts to move downward, and the surge is more notable under a lower hot flue gas pressure. This phenomenon can be explained as follows: the original balanced state at the solid−liquid−gas three-phase contact line is destructed when droplets start to move, which triggers a change in the interaction energy at the interface.[48,49] After the surge, an obvious inflection point turns up, marking the slowing down of the increase rate. As the coal substrate and water droplets continue to move downward, the interaction energy basically stabilizes under different pressures. After the stabilization, the absolute value of the interaction energy keeps decreasing with the rise of pressure, which stands for the

https://doi.org/10.1021/acsomega.4c06994
ACS Omega 2024, 9, 44577−44587

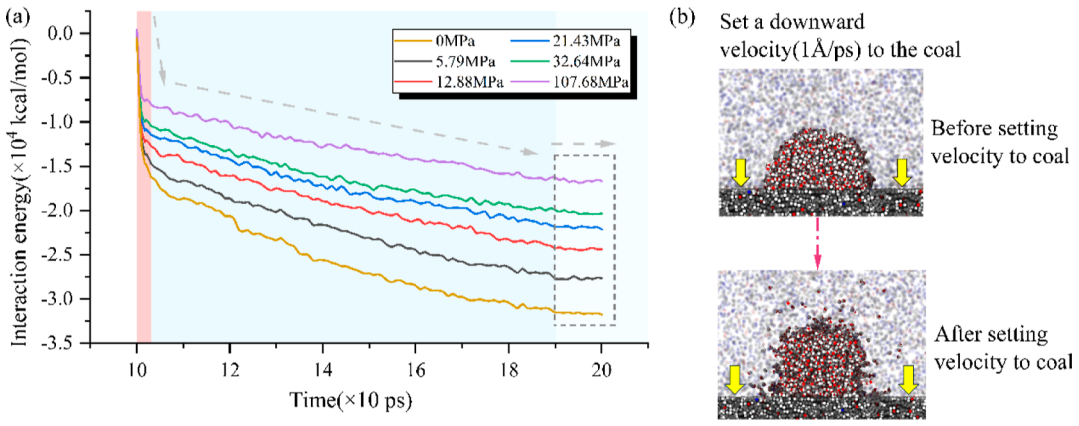

Figure 5. (a) Interaction energy under different pressures. (b) Before and after the velocity is set to the coal base.

weakening of the wetting effect of water nanodroplets on the coal substrate.

With the intention of further illustrating the connection between the coal substrate and water, the average interaction energy in the last 10 ps under different pressures is calculated

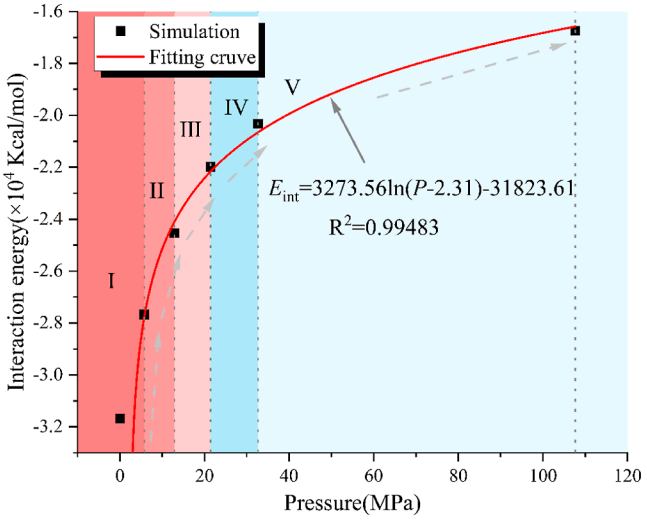

Figure 6. Average interaction energy in the last 10 ps under different pressures.

and fitted into a curve. As presented in Figure 6, interaction energy and pressure satisfy a logarithmic relationship

$$E_{int} = a\ln(P - b) - c \quad (6)$$

where E_{int} is the interaction energy; P is the hot flue gas injection pressure; a, b, and c are constants related to coal rank, surface functional group type, etc. On the whole, the gradient of decrease in interaction energy shrinks continuously when the pressure rises. This law is reflected in Figure 6: when the pressure increases from 0 to 5.79 MPa, from 5.79 to 12.88 MPa, from 12.88 to 21.43 MPa, from 21.43 to 32.64 MPa, and from 32.64 to 107.68 MPa, the interaction energy drops by 4003.15, 3143.49, 2549.03, 1659.17, and 3582.72 kcal/mol, respectively.

3.2. Number of Hydrogen Bonds. The hydrogen bonds formed between water molecules and oxygen-containing functional groups on the surface of the coal substrate, such as hydroxyl, carboxyl, and other highly electronegative nitrogen atoms enable water droplets to better spread on the coal substrate. As a general rule, energy and geometric criteria are used to determine the existence of hydrogen bonds. In this paper, the Luzar Chandler criterion[50] is adopted to explore the relationship between the pressure P and the statistical average number of hydrogen bonds at the coal−water interface during the last 2 ns. The curve in Figure 7 provides the information that

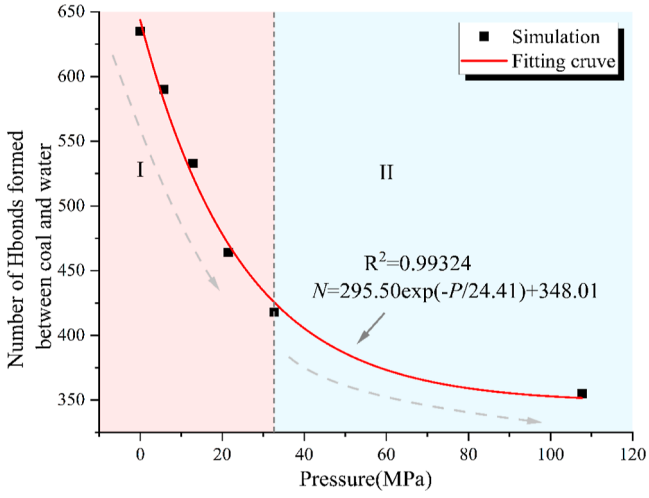

Figure 7. Changes in number of hydrogen bonds between coal and water under different pressures.

the number of hydrogen bonds between coal and water experience a dramatic drop as the pressure mounts up, which agrees with the finding by Zhou et al.[44] For instance, it drops from 635 at 0 MPa to 533 at 12.88 MPa. As the pressure continues to rise, it reaches as low as 355 at 107.68 MPa, a drop of 44.09% compared to 635 at 0 MPa. Such a drop is indicative of the weakening of the wetting effect of water nanodroplets on the coal substrate. Furthermore, the fitting curve displays an exponential relationship between the number of hydrogen bonds and the pressure

$$N = de^{(-P/f)} + g \quad (7)$$

where N is the number of hydrogen bonds; P is the hot flue gas injection pressure; and d, f, and g are constants related to coal rank, surface functional group types, etc.

At the critical point of 32.64 MPa, the downward trend of hydrogen bonds takes on a transition. When $P < 32.64$ MPa, the number of hydrogen bonds is more sensitive to pressure

https://doi.org/10.1021/acsomega.4c06994
ACS Omega 2024, 9, 44577−44587

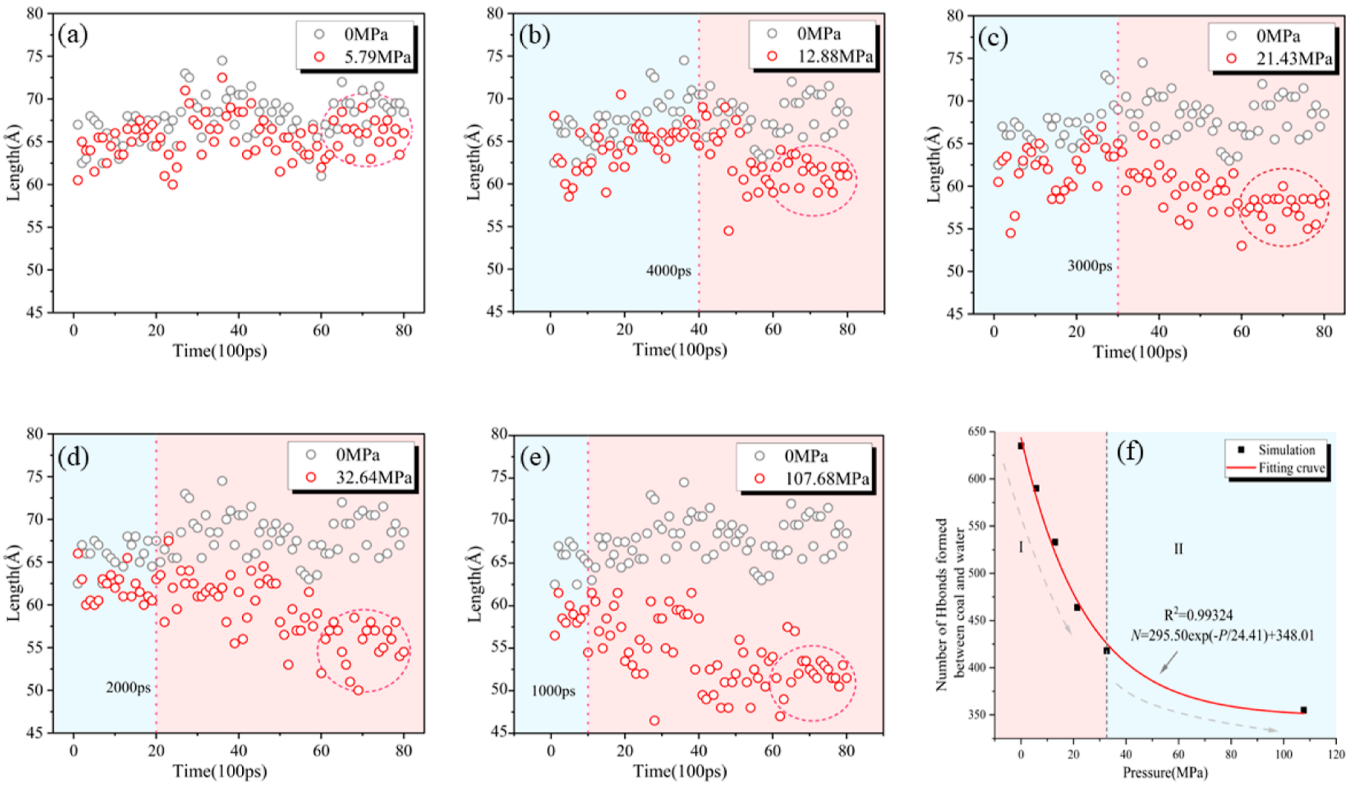

Figure 8. Spreading length of water nanodroplets in the *X*-direction under different pressures. (a) 0 and 5.79 MPa. (b) 0 and 12.88 MPa. (c) 0 and 21.43 MPa. (d) 0 and 32.64 MPa. (e) 0 and 107.68 MPa. (f) Fitting curve.

changes, decreasing by 217 under a pressure difference of 32.64 MPa. When $P > 32.64$ MPa, the number of hydrogen bonds only decreases by 63 under a pressure difference of 75.04 MPa.

Based on analysis in Section 3.1, it can be concluded that the formation of hydrogen bonds between coal and water conduces to coal−water interactions. Under a lower pressure, more hydrogen bonds are formed between coal and water, bringing about an increased absolute value of interaction energy. When $P = 0$ MPa, the number of hydrogen bonds marks 655, and the corresponding absolute value of interaction energy is calculated to be 31,675.13 kcal/mol. However, when $P = 107.68$ MPa, the number of hydrogen bonds becomes only 355, and the absolute value of interaction energy falls to 16,740.64 kcal/mol at this time.

3.3. Spreading Length (Effective Contact Area). In this study, a semicircular water nanodroplet with a centerline length and radius of 5 nm is prepared for wettability simulation under different pressures. The spread lengths of water nanodroplets in the *X*-direction under different pressures after relaxation are detailed in Figure 8. As can be known from Figure 8, when $P = 5.79$ MPa, the spreading length of water nanodroplets in the *X*-direction varies in similar trends to that when $P = 0$ MPa. However, its overall value is slightly lower than that when $P = 0$ MPa at the same time, which is particularly apparent in the last 2 ns of the simulation. When $P > 5.79$ MPa, the spreading length of water nanodroplets in the *X*-direction varies in different trends from that at $P = 0$ MPa, and such a phenomenon is more conspicuous under a higher pressure *P*. As shown in Figure 8b−e, when $P > 5.79$ MPa, the variation of spreading length experiences a turning point. The spreading length decrease noticeably in the period between the turning point and the spreading length stabilization. The time when the turning point appears is found to be negatively correlated with pressure. That is to say, the higher the pressure, the earlier the turning point appears, and vice versa. Specifically, the turning point appears near 4000 ps under a pressure of 12.88 MPa; it occurs 1000 ps earlier when the pressure rises to 21.43 MPa; and a noticeable turning point is tracked around 1000 ps under 107.68 MPa, an increase of 75% compared to the case under 5.79 MPa.

In a bid to uncover the relationship between the spreading length in the *X*-direction and the pressure, the average values of the spreading length in the last 2 ns under different pressures are calculated, and curve fitting is performed. The results are illustrated in Figure 8f. As a whole, a negative exponential relationship exists between the spreading length *L* and the pressure *P*

$$L = he^{(-P/i)} + g \tag{8}$$

where *h*, *i*, and *g* are constants related to coal rank, surface functional group type, etc.

Similar to the variation trend of hydrogen bonds, the curve of the spreading length in the *X*-direction also varies in two different trends, divided by around 32.64 MPa. When $P < 32.64$ MPa, the spreading length is more sensitive to the rise of pressure, evidenced by the phenomenon that it decreases from 6.85 to 5.57 nm under a pressure difference of 32.64 MPa. In contrast, when $P > 32.64$ MPa, it only declines by 0.41 nm under a pressure difference of 75.04 MPa. These behaviors explain that the variation trend of spreading length with pressure is well correlated with the variation trends of number of hydrogen bonds and interaction energy with pressure, which indicates that a longer spreading length is usually accompanied by more hydrogen bonds and stronger interactions.

3.4. Contact Angle. The two-dimensional (2D) density contour maps of stable water droplets under different pressures,

https://doi.org/10.1021/acsomega.4c06994
ACS Omega 2024, 9, 44577−44587

acquired by statistically averaging the density distribution data in the last 2 ns, are exhibited in Figure 9. Based on each contour

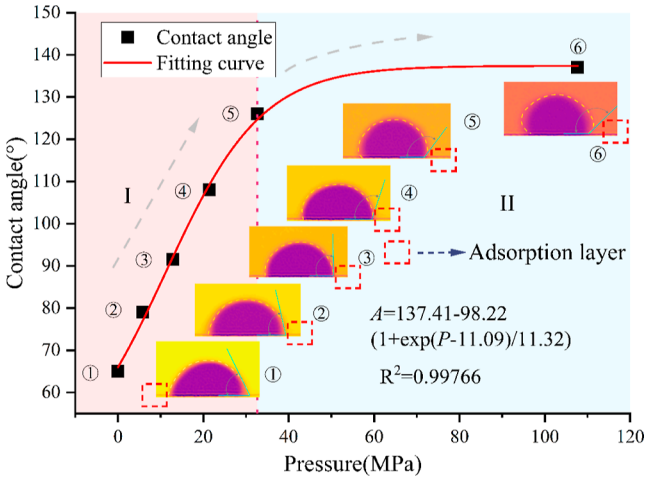

Figure 9. Variation trend of contact angle under different hot flue gas injection pressures.

map, the droplet profile is further fitted. Subsequently, the corresponding contact angle is calculated from the angle between the tangent of the water nanodroplet and the coal substrate surface. As depicted in Figure 9, the contact angle keeps growing with the rise of pressure. To be specific, it grows from 65.2° at 0 MPa to 79.7° at 5.79 MPa, 91.6° at 12.88 MPa, 108.3° at 21.43 MPa, 126.5° at 32.64 MPa, and 137.1° at 107.68 MPa. On the coal substrate surface, a distinct gas adsorption layer that is susceptible to the hot flue gas injection pressure is observed on both sides of the water droplet. As the pressure rises, the density of the adsorption layer also presents a sustained increase. The variations of both the contact angle and the adsorption layer density discloses that the wetting effect of water on the coal substrate deteriorates as the pressure goes up, accompanied by a transition of wetting mode from water wetting to gas wetting.

In the hope of figuring out the dependence of contact angle on pressure, fitting is performed on the variation trend of contact angle with pressure, and the fitting result shows an exponential relationship between them

$$\theta = k - m(1 + e^{(P-n)/s}) \quad (9)$$

where θ is the contact angle; P is the hot flue gas injection pressure; and k, m, n, and s are constants related to coal rank, surface functional group type, etc. In Figure 9, it is clear that the variation consists of two stages, I and II, divided by 32.64 MPa. When P < 32.64 MPa, how the contact angle changes depends more on the pressure, reflected in the phenomenon that the contact angle experiences an abrupt increase from 65.4 to 126.5° as the pressure rises from 0 to 32.64 MPa. When P > 32.64 MPa, the contact angle is less sensitive to pressure. For instance, it only grows by 10.6° when the pressure enlarges from 32.64 to 107.69 MPa.

In addition, it is identified that the increase in contact angle brought by the pressure increase of hot flue gas injection is smaller than that brought by pure CO_2 injection, which agrees with the experimental results obtained by Kaveh et al.[16] Such a result may be attributed to the lower concentration of CO_2 in hot flue gas. It is generally acknowledged that CO_2 competes intensely with water for wettability on the coal substrate through three mechanisms: (1) The increase in CO_2 concentration leads to the intensification of CO_2−H_2O interactions,[51,52] which further promotes surface tension of water molecules;[53] (2) The adsorption capacity of CO_2 on the coal substrate grows with the rise of pressure;[54−58] (3) The increased solubility of CO_2 in water results in a raised H^+ concentration, which in turn enhances the wettability of CO_2.[59]

The molecular "invasion" phenomenon is captured at the gas−liquid interface under different pressures (Figure 10). When $P \geq$ 32.64 MPa, such a phenomenon is much more pronounced, destabilizing the interface between water nanodroplets and hot flue gas, which coincides with the phenomenon observed in pictures ⑤, ⑥, in Figure 9. This phenomenon has something to do with the increased solubility of gas molecules in the water nanodroplet under a high pressure. Gas molecules dissolved on the water nanodroplet surface possess a molecular structure different from that of pure water, which further induces differences in density distribution between the surface and interior of the water nanodroplet.

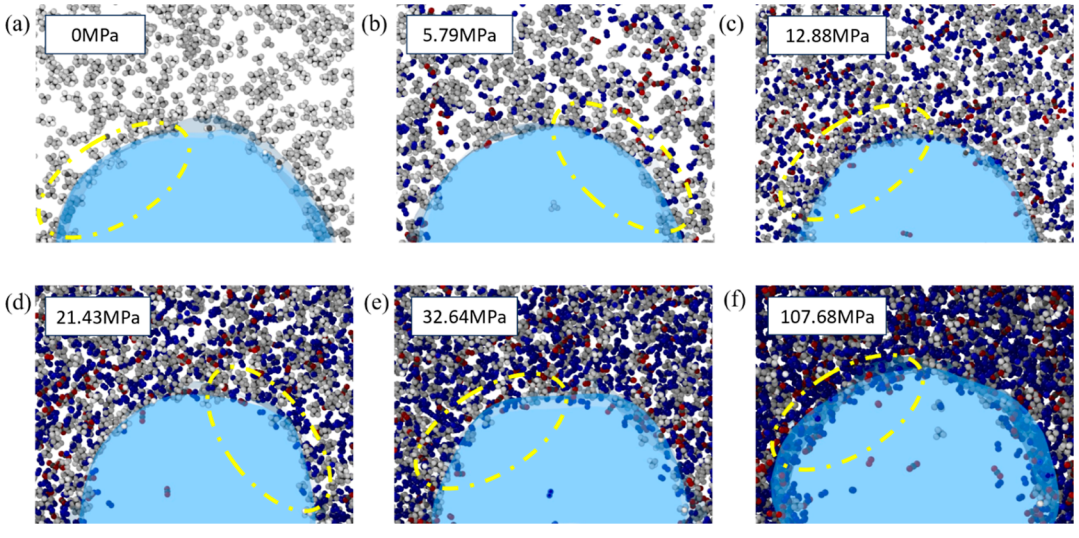

Figure 10. Molecular "invasion" under different pressures. (a) 0 MPa. (b) 5.79 MPa. (c) 12.88 MPa. (d) 21.43 MPa. (e) 32.64 MPa. (f) 107.68 MPa.

https://doi.org/10.1021/acsomega.4c06994
ACS Omega 2024, 9, 44577−44587

4. CONCLUSIONS

In this paper, a multicomponent wetting model of coal−water−methane−hot flue gas was constructed. With this model, how the interaction energy, the spreading length of water nanodroplets and the contact angle vary with the hot flue gas injection pressure. The primary conclusions drawn are as follows.

(1) The comparison between the system pressure obtained by NIST and the calculated principal stresses calculated by LAMMPS reveals that the deviation is less than 5% even under extremely high molecular densities. This finding proves that it is feasible to adopt the NIST method to obtain system pressure.

(2) The interaction energy and the hot flue gas injection pressure follow a logarithmic relationship, and the gradient of decrease in interaction energy shrinks continuously with the rise of pressure. For example, the interaction energy plunges by 11,351.71 kcal/mol when the pressure increases from 0 to 32.64 MPa, and it declines by merely 3582.77 kcal/mol when the pressure climbs up from 32.64 to 107.68 MPa.

(3) The variations of number of hydrogen bonds between coal and water and spreading length of water nanodroplets with pressure comprises two stages, divided by a critical value of 32.64 MPa. When the pressure rises from 0 to 32.64 MPa, the number of hydrogen bonds falls from 635 to 418, by 34.17%, and the spreading length decreases from 6.85 to 5.57 nm, by 18.69%. In contrast, when the pressure rises from 32.64 to 107.68 MPa, the number of hydrogen bonds undergoes a decrease from 418 to 355, by 15.07%, and the spreading length also experiences a reduction from 5.57 to 5.17 nm, by 7.18%.

(4) As the pressure increases, both the contact angle and the density of the gas adsorption layer on both sides of the water droplet multiply. Specifically, the contact angle enlarges from 65 to 137° when the pressure rises from 0 to 107.68 MPa. Their variations indicate that appropriately raising the injection hot flue gas injection pressure can promote the transition of wetting mode from water wetting to gas wetting. Under pressures greater than 32.64 MPa, the molecular "invasion" phenomenon caused by increased solubility becomes more conspicuous.

AUTHOR INFORMATION

Corresponding Authors

Baiquan Lin − *Key Laboratory of Theory and Technology on Coal and Rock Dynamic Disaster Prevention and Control, National Mine Safety Administration, China University of Mining and Technology, Xuzhou 221116, China; School of Safety Engineering, China University of Mining and Technology, Xuzhou, Jiangsu 221116, China; Key Laboratory of Coalbed Methane Resources and Reservoir Formation Process, Ministry of Education, China University of Mining and Technology, Xuzhou 221008, China;* orcid.org/0000-0002-2794-6707; Email: lbq21405@126.com

Xiangliang Zhang − *Key Laboratory of Theory and Technology on Coal and Rock Dynamic Disaster Prevention and Control, National Mine Safety Administration, China University of Mining and Technology, Xuzhou 221116, China; School of Safety Engineering, China University of Mining and Technology, Xuzhou, Jiangsu 221116, China; Key Laboratory of Coalbed Methane Resources and Reservoir Formation Process, Ministry of Education, China University of Mining and Technology, Xuzhou 221008, China*; Email: xl_zhang0719@cumt.edu.cn

Authors

Shunqing Ma − *Key Laboratory of Theory and Technology on Coal and Rock Dynamic Disaster Prevention and Control, National Mine Safety Administration, China University of Mining and Technology, Xuzhou 221116, China; School of Safety Engineering, China University of Mining and Technology, Xuzhou, Jiangsu 221116, China; Key Laboratory of Coalbed Methane Resources and Reservoir Formation Process, Ministry of Education, China University of Mining and Technology, Xuzhou 221008, China;* orcid.org/0009-0003-3091-2385

Qian Liu − *School Resource Engineering, Longyan University, Longyan, Fujian 364012, P. R. China*

Wei Zha − *Key Laboratory of Theory and Technology on Coal and Rock Dynamic Disaster Prevention and Control, National Mine Safety Administration, China University of Mining and Technology, Xuzhou 221116, China; School of Safety Engineering, China University of Mining and Technology, Xuzhou, Jiangsu 221116, China; Key Laboratory of Coalbed Methane Resources and Reservoir Formation Process, Ministry of Education, China University of Mining and Technology, Xuzhou 221008, China*

Complete contact information is available at: https://pubs.acs.org/10.1021/acsomega.4c06994

Notes

The authors declare no competing financial interest.

ACKNOWLEDGMENTS

This work was financed by National Natural Science Foundation of China (52334007, 52304269), Natural Science Foundation of Jiangsu Province (BK20221122).

REFERENCES

(1) Espinoza, D. N.; Pereira, J. M.; Vandamme, M.; Dangla, P.; Vidal-Gilbert, S. Desorption-induced shear failure of coal bed seams during gas depletion. *Int. J. Coal Geol.* **2015**, *137*, 142−151.

(2) Guanhua, N.; Hongchao, X.; Shang, L.; Qian, S.; Dongmei, H.; Yanying, C.; Ning, W. The effect of anionic surfactant (SDS) on pore-fracture evolution of acidified coal and its significance for coalbed methane extraction. *Adv. Powder Technol.* **2019**, *30* (5), 940−951.

(3) Liu, H. B.; Cheng, Y. P. The elimination of coal and gas outburst disasters by long distance lower protective seam mining combined with stress-relief gas extraction in the Huaibei coal mine area. *J. Nat. Gas Sci. Eng.* **2015**, *27*, 346−353.

(4) Liu, Y.; Zhou, F.; Wang, J.; Liu, J. Approach to increasing the quality of pressure-relieved gas drained from protected coal seam using surface borehole and its industrial application. *Int. J. Coal Sci. Technol.* **2015**, *2* (1), 46−51.

(5) Zhou, L.; Su, X. P.; Lu, Y. Y.; Ge, Z. L.; Zhang, Z. Y.; Shen, Z. H. A New Three-Dimensional Numerical Model Based on the Equivalent Continuum Method to Simulate Hydraulic Fracture Propagation in an Underground Coal Mine. *Rock Mech. Rock Eng.* **2019**, *52* (8), 2871−2887.

(6) Zhang, X.; Ranjith, P. G. Experimental investigation of effects of CO2 injection on enhanced methane recovery in coal seam reservoirs. *J. CO2 Util.* **2019**, *33*, 394−404.

(7) Mohamed, T.; Mehana, M. CoalBed methane characterization and modeling: review and outlook. *Energy Sources Part A* **2020**, *42*, 1−23.

(8) Aminu, M. D.; Nabavi, S. A.; Rochelle, C. A.; Manovic, V. A review of developments in carbon dioxide storage. *Appl. Energy* **2017**, *208*, 1389−1419.

https://doi.org/10.1021/acsomega.4c06994
ACS Omega 2024, 9, 44577−44587

(9) Wu, S. Y.; Deng, C. B.; Wang, X. F. Molecular simulation of flue gas and CH_4 competitive adsorption in dry and wet coal. *J. Nat. Gas Sci. Eng.* **2019**, *71*, 102980.
(10) Mukherjee, M.; Misra, S. A review of experimental research on Enhanced Coal Bed Methane (ECBM) recovery via CO_2 sequestration. *Earth-Sci. Rev.* **2018**, *179*, 392−410.
(11) Cracknell, R. F.; Nicholson, D.; Tennison, S. R.; Bromhead, J. Adsorption and selectivity of carbon dioxide with methane and nitrogen in slit-shaped carbonaceous micropores: Simulation and experiment. *Adsorption* **1996**, *2* (3), 193−203.
(12) Jessen, K.; Tang, G. Q.; Kovscek, A. R. Laboratory and simulation investigation of enhanced coalbed methane recovery by gas injection. *Transp. Porous Media* **2008**, *73* (2), 141−159.
(13) Wang, J. M.; Zhao, Y. S.; Mao, R. B. Impact of temperature and pressure on the characteristics of two-phase flow in coal. *Fuel* **2019**, *253*, 1325−1332.
(14) Su, X.; Feng, Z.; Cai, T.; Shen, Y. Coal Permeability Variation during the Heating Process considering Thermal Expansion and Desorption Shrinkage. *Adsorpt. Sci. Technol.* **2022**, *2022*, 7848388.
(15) Chen, K.; Liu, X. F.; Nie, B. S.; Zhang, C. P.; Song, D. Z.; Wang, L. K.; Yang, T. Mineral dissolution and pore alteration of coal induced by interactions with supercritical CO_2. *Energy* **2022**, *248*, 123627.
(16) Kaveh, N. S.; Rudolph, E. S. J.; Wolf, K.; Ashrafizadeh, S. N. Wettability determination by contact angle measurements: hvbB coal-water system with injection of synthetic flue gas and CO_2. *J. Colloid Interface Sci.* **2011**, *364* (1), 237−247.
(17) Zhao, J.; Tian, S.; Jiang, Z.; Li, P.; Li, Z.; Gou, R.; Ma, T. Study on the mechanism of SiO2-H2O nanofluid enhanced water injection in coal seam. *Appl. Surf. Sci.* **2024**, *658*, 159843.
(18) Zhao, J.; Tian, S.; Li, P.; Xie, H.; Cai, J. Molecular dynamics simulation and experimental research on the influence of SiO_2-H_2O nanofluids on wettability of low-rank coal. *Colloids Surf., A* **2023**, *679*, 132580.
(19) Mayo, S. L.; Olafson, B. D.; Goddard, W. A. DREIDING: a generic force field for molecular simulations. *J. Phys. Chem.* **1990**, *94* (26), 8897−8909.
(20) Nosé, S. A unified formulation of the constant temperature molecular dynamics methods. *J. Chem. Phys.* **1984**, *81* (1), 511−519.
(21) Wu, S.; Jin, Z.; Deng, C. Molecular simulation of coal-fired plant flue gas competitive adsorption and diffusion on coal. *Fuel* **2019**, *239*, 87−96.
(22) Li, J.; Wang, Y.; Chen, Z.; Rahman, S. S. Effects of moisture, salinity and ethane on the competitive adsorption mechanisms of CH_4/CO_2 with applications to coalbed reservoirs: A molecular simulation study. *J. Nat. Gas Sci. Eng.* **2021**, *95*, 104151.
(23) Xiang, J.-h.; Zeng, F.-g.; Li, B.; Zhang, L.; Li, M.-f.; Liang, H.-z. Construction of macromolecular structural model of anthracite from Chengzhuang coal mine and its molecular simulation. *J. Fuel Chem. Technol.* **2013**, *41* (4), 391−400.
(24) Berendsen, H. J. C.; Grigera, J. R.; Straatsma, T. P. The missing term in effective pair potentials. *J. Phys. Chem.* **1987**, *91* (24), 6269−6271.
(25) Yang, Y.; Che Ruslan, M. F. A.; Narayanan Nair, A. K.; Qiao, R.; Sun, S. Interfacial properties of the hexane + carbon dioxide + water system in the presence of hydrophilic silica. *J. Chem. Phys.* **2022**, *157*(23), 234704.
(26) Chen, F.; Smith, P. E. Simulated surface tensions of common water models. *J. Chem. Phys.* **2007**, *126*(22), 221101.
(27) Jorgensen, W. L.; Maxwell, D. S.; Tirado-Rives, J. Development and Testing of the OPLS All-Atom Force Field on Conformational Energetics and Properties of Organic Liquids. *J. Am. Chem. Soc.* **1996**, *118* (45), 11225−11236.
(28) Zhu, A.; Zhang, X.; Liu, Q.; Zhang, Q. A Fully Flexible Potential Model for Carbon Dioxide. *Chin. J. Chem. Eng.* **2009**, *17* (2), 268−272.
(29) Aimoli, C. G.; Maginn, E. J.; Abreu, C. R. A. Force field comparison and thermodynamic property calculation of supercritical CO_2 and CH_4 using molecular dynamics simulations. *Fluid Phase Equilib.* **2014**, *368*, 80−90.
(30) Stubbs, J. M. Molecular simulations of supercritical fluid systems. *J. Supercrit. Fluids* **2016**, *108*, 104−122.
(31) Hoover, W. Canonical Dynamics: Equilibrium Phase-Space Distributions. *Phys. Rev. A: At., Mol., Opt. Phys.* **1985**, *31*, 1695−1697.
(32) Scocchi, G.; Sergi, D.; D'Angelo, C.; Ortona, A. Wetting and contact-line effects for spherical and cylindrical droplets on graphene layers: A comparative molecular-dynamics investigation. *Phys. Rev. E* **2011**, *84* (6), 061602.
(33) Plimpton, S. Fast Parallel Algorithms for Short-Range Molecular Dynamics. *J. Comput. Phys.* **1995**, *117* (1), 1−19.
(34) Kräutler, V.; van Gunsteren, W. F.; Hünenberger, P. H. A fast SHAKE algorithm to solve distance constraint equations for small molecules in molecular dynamics simulations. *J. Comput. Chem.* **2001**, *22* (5), 501−508.
(35) Jones, J. E.; Chapman, S. On the determination of molecular fields. -II. From the equation of state of a gas. *Proc. R. Soc. Lond.* **1924**, *106* (738), 463−477.
(36) Brown, W. M.; Kohlmeyer, A.; Plimpton, S. J.; Tharrington, A. N. Implementing molecular dynamics on hybrid high performance computers - Particle-particle particle-mesh. *Comput. Phys. Commun.* **2012**, *183* (3), 449−459.
(37) Ghoufi, A.; Malfreyt, P. Importance of the tail corrections on surface tension of curved liquid-vapor interfaces. *J. Chem. Phys.* **2017**, *146*(8), 084703.
(38) MacDowell, L. G.; Blas, F. J. Surface tension of fully flexible Lennard-Jones chains: Role of long-range corrections. *J. Chem. Phys.* **2009**, *131*(7), 074705.
(39) Lundberg, L.; Edholm, O. Dispersion Corrections to the Surface Tension at Planar Surfaces. *J. Chem. Theory Comput.* **2016**, *12* (8), 4025−4032.
(40) Jablonka, K. M.; Ongari, D.; Smit, B. Applicability of Tail Corrections in the Molecular Simulations of Porous Materials. *J. Chem. Theory Comput.* **2019**, *15* (10), 5635−5641.
(41) Schlaich, A.; Coasne, B. Dispersion truncation affects the phase behavior of bulk and confined fluids: Coexistence, adsorption, and criticality. *J. Chem. Phys.* **2019**, *150*(15), 154104.
(42) Míguez, J. M.; Piñeiro, M. M.; Blas, F. J. Influence of the long-range corrections on the interfacial properties of molecular models using Monte Carlo simulation. *J. Chem. Phys.* **2013**, *138*(3), 034707.
(43) Jagadisan, A.; Heidari, Z. Molecular dynamic simulation of the impact of thermal maturity and reservoir temperature on the contact angle and wettability of kerogen. *Fuel* **2022**, *309*, 122039.
(44) Zhou, J.; Zhang, J. J.; Yang, J. P.; Jin, Z. H.; Luo, K. H. Mechanisms for kerogen wettability transition from water-wet to CO_2-wet: Implications for CO_2 sequestration. *Chem. Eng. J.* **2022**, *428*, 132020.
(45) Zhang, X. Y.; Kang, T. H.; Zhang, B.; Kang, G. X.; Kang, J. T.; Zhang, R. X.; Zhang, L. K. Combined Molecular Simulations and Experimental Study of Methane Adsorption on Anthracite. *Energy Fuels* **2020**, *34* (10), 12118−12125.
(46) Huang, L.; Ning, Z. F.; Wang, Q.; Zhang, W. T.; Cheng, Z. L.; Wu, X. J.; Qin, H. B. Effect of organic type and moisture on CO_2/CH_4 competitive adsorption in kerogen with implications for CO_2 sequestration and enhanced CH_4 recovery. *Appl. Energy* **2018**, *210*, 28−43.
(47) Yu, S.; Bo, J.; Wu, L. Molecular simulation of CH_4/CO_2/H_2O competitive adsorption on low rank coal vitrinite. *Phys. Chem. Chem. Phys.* **2017**, *19* (27), 17773−17788.
(48) Yang, Y. F.; Narayanan Nair, A. K.; Zhu, W. W.; Sang, S. X.; Sun, S. Y. Molecular perspectives of interfacial properties of the hydrogen +water mixture in contact with silica or kerogen. *J. Mol. Liq.* **2023**, *385*, 122337.
(49) Yang, Y. F.; Che Ruslan, M. F. A.; Narayanan Nair, A. K.; Qiao, R.; Sun, S. Y. Interfacial properties of the hexane + carbon dioxide + water system in the presence of hydrophilic silica. *J. Chem. Phys.* **2022**, *157*(23), 234704.
(50) Luzar, A.; Chandler, D. Structure and hydrogen bond dynamics of water−dimethyl sulfoxide mixtures by computer simulations. *J. Chem. Phys.* **1993**, *98* (10), 8160−8173.

https://doi.org/10.1021/acsomega.4c06994
ACS Omega 2024, 9, 44577−44587

(51) Arif, M.; Al-Yaseri, A. Z.; Barifcani, A.; Lebedev, M.; Iglauer, S. Impact of pressure and temperature on CO_2−brine−mica contact angles and CO_2−brine interfacial tension: Implications for carbon geo-sequestration. *J. Colloid Interface Sci.* **2016**, *462*, 208−215.
(52) Iglauer, S.; Mathew, M. S.; Bresme, F. Molecular dynamics computations of brine-CO_2 interfacial tensions and brine-CO_2-quartz contact angles and their effects on structural and residual trapping mechanisms in carbon geo-sequestration. *J. Colloid Interface Sci.* **2012**, *386*, 405−414.
(53) Cho, C. H.; Urquidi, J.; Singh, S.; Park, S. C.; Robinson, G. W. Pressure effect on the density of water. *J. Phys. Chem. A* **2002**, *106* (33), 7557−7561.
(54) Krooss, B. M.; van Bergen, F.; Gensterblum, Y.; Siemons, N.; Pagnier, H. J. M.; David, P. High-pressure methane and carbon dioxide adsorption on dry and moisture-equilibrated Pennsylvanian coals. *Int. J. Coal Geol.* **2002**, *51* (2), 69−92.
(55) Bae, J. S.; Bhatia, S. K. High-pressure adsorption of methane and carbon dioxide on coal. *Energy Fuels* **2006**, *20* (6), 2599−2607.
(56) Fitzgerald, J. E.; Pan, Z.; Sudibandriyo, M.; Robinson Jr, R.; Gasem, K. A. M.; Reeves, S. Adsorption of methane, nitrogen, carbon dioxide and their mixtures on wet Tiffany coal. *Fuel* **2005**, *84* (18), 2351−2363.
(57) Li, D.; Liu, Q.; Weniger, P.; Gensterblum, Y.; Busch, A.; Krooss, B. M. High-pressure sorption isotherms and sorption kinetics of CH4 and CO2 on coals. *Fuel* **2010**, *89* (3), 569−580.
(58) Siemons, N.; Busch, A. Measurement and interpretation of supercritical CO_2 sorption on various coals. *Int. J. Coal Geol.* **2007**, *69* (4), 229−242.
(59) Ibrahim, A. F.; Nasr-El-Din, H. A. Effect of Water Salinity on Coal Wettability During CO_2 Sequestration in Coal Seams. *Energy Fuels* **2016**, *30* (9), 7532−7542.

https://doi.org/10.1021/acsomega.4c06994
ACS Omega 2024, 9, 44577−44587